

Supporting information

Mixed-Cation Vacancy-Ordered Perovskites ($\text{Cs}_2\text{Ti}_{1-x}\text{Sn}_x\text{X}_6$; X = I, Br); Low Temperature Miscibility, Additivity and Tunable Stability

Shanti M. Liga^{a,‡}, Seán R. Kavanagh^{b,c,‡}, Aron Walsh^{c,d}, David O. Scanlon^b & Gerasimos Konstantatos^{a,e,*}

^aICFO-Institut de Ciències Fotòniques, The Barcelona Institute of Science and Technology, 08860 Castelldefels (Barcelona), Spain

^bThomas Young Centre and Department of Chemistry, University College London, London, UK

^cThomas Young Centre and Department of Materials, Imperial College London, London, UK

^d Department of Physics, Ewha Womans University, Seoul 03760, Korea

^eICREA-Institució Catalana de Recerca i Estudis Avancats, Passeig Lluís Companys 23, 08010 Barcelona, Spain

#These authors contributed equally: Shanti M. Liga, Seán R. Kavanagh

* Corresponding author, e-mail: gerasimos.konstantatos@icfo.es

Experimental section.

X-ray Diffraction (XRD) characterization. XRD patterns were collected using a Rigaku SmartLab diffractometer in Bragg-Brentano $\Theta/2\Theta$ geometry, Cu $\text{k}\alpha$ radiation (wavelength=1.5406 \AA) and a D/teX Ultra 250 silicon strip detector. The NCs samples were prepared by drop casting the nanocrystals' solutions on the top of a silicon wafer. For the characterization, all the samples were measured inside an air-sensitive sample holder, which was loaded in the glovebox to avoid any contact with air, while for the stability study, they were exposed to air.

Transmission Electron Microscopy (TEM) characterization. TEM measurements were performed at the Scientific and Technological Centres of the University of Barcelona (CCiT-UB). TEM images were acquired in a JEOL J2010F TEM microscope, equipped with a field emission electron gun (FEG). The microscope was operated at an accelerating voltage of 200 kV. Samples for TEM characterization were prepared in the glovebox by drop-casting diluted toluene solutions (50 μL of NCs solution in 1 ml of toluene) onto 200 mesh carbon-coated copper grids.

ICP-OES measurements. ICP-OES measurements were performed at the Scientific and Technological Centres of the University of Barcelona (CCiT-UB). Elemental analysis of the samples was carried out using an ICP-OES PerkinElmer, model Optima 3200RL, in standard conditions. The digestion of the sample necessary for this measurement was carried out by adding to the dry NCs obtained from 2.5 ml of the washed solution, 6 ml of HNO₃, 2 ml of H₂O₂, 1 ml of HF and deionized water, and heating the solution at 210 °C at high pressure in a microwave digestion system “Milestone EthosOne”.

UV-vis Absorption measurements. Optical absorption spectra were collected using a Varian Cary-5000 UV-vis-NIR spectrophotometer.

Sample name	Cs	Sn	Ti	I
Cs_2TiI_6	2	0	2.5	27
25% Sn	2	0.25	1.875	27
50% Sn	2	0.5	1.25	27
75% Sn	2	0.75	0.625	27
Cs_2SnI_6	2	1	0	6

Table S1. Summary of the precursor ratios used to synthesize $\text{Cs}_2\text{Ti}_{1-x}\text{Sn}_x\text{I}_6$ alloys.

Sample name	$a = b = c /(\text{\AA})$	Rwp (%)	χ^2
Cs_2TiBr_6	10.706(3)	10.11	2.75
10% Sn	10.761(5)	3.35	1.56
20% Sn	10.800(2)	3.53	1.78
30% Sn	10.819(6)	4.34	2.92
50% Sn	10.831(4)	5.79	4.75
Cs_2SnBr_6	10.840(3)	7.57	1.81
Cs_2TiI_6	11.468(5)	5.90	7.28
25% Sn	11.537(4)	5.96	2.52
50% Sn	11.5730(14)	8.05	1.64
75% Sn	11.594(5)	7.89	1.53
Cs_2SnI_6	11.6786(10)	6.45	1.44

Table S2. Rietveld refinement parameters (lattice parameter, weighted-profile R-factor (Rwp) and goodness of fit (χ^2) values) for all the samples.

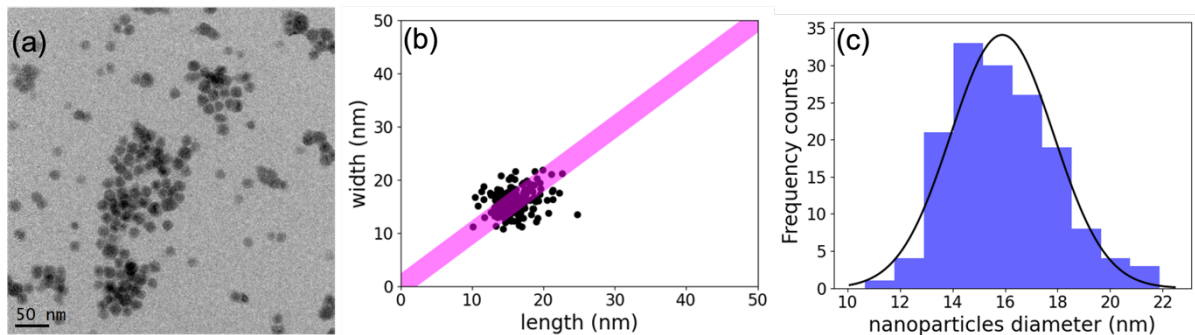


Figure S1. (a) TEM image of Cs_2SnI_6 NCs prepared at 140 °C. (b) Plot of the width vs the length of the NCs. (c) Histogram of the NCs diameters, calculated from the area of the NCs, indicating an average NC diameter of 15.9 nm, with a standard deviation of around 2.0 nm.

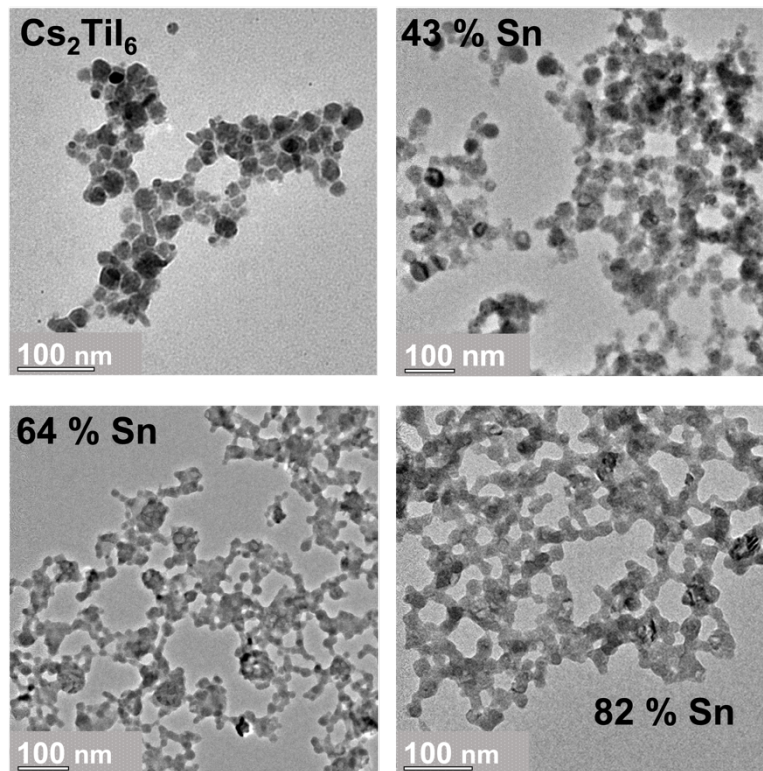


Figure S2. TEM images of Cs_2TiI_6 and $\text{Cs}_2\text{Ti}_{1-x}\text{Sn}_x\text{I}_6$ with $x = 0.43, 0.64$ and 0.82 . In these samples the coalescence and agglomeration of the NCs did not allow a size distribution analysis to be performed. TEM images of these samples show NCs with asymmetrical shapes and different sizes.

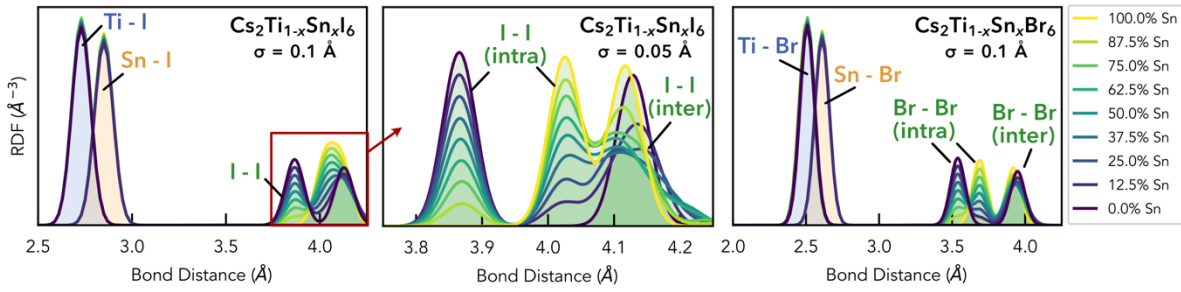


Figure S3. Calculated Radial Distribution Functions (RDFs) of the Ti-X, Sn-X and X-X ($X = I, Br$) atomic distances in $Cs_2Ti_{1-x}Sn_xI_6$ and $Cs_2Ti_{1-x}Sn_xBr_6$ perovskites. “intra” and “inter” refer to intra-octahedral and inter-octahedral X-X distances respectively. For $Cs_2Ti_{1-x}Sn_xI_6$, the small difference between intra-octahedral SnI_6 I-I distances and inter-octahedral I-I distances ($\sim 0.1 \text{ \AA}$) results in merged RDF peaks, and so a zoomed inset with a reduced peak broadening ($\sigma = 0.05 \text{ \AA}$) is shown in the middle subplot to distinguish these peaks. RDFs calculated using vasppy.³

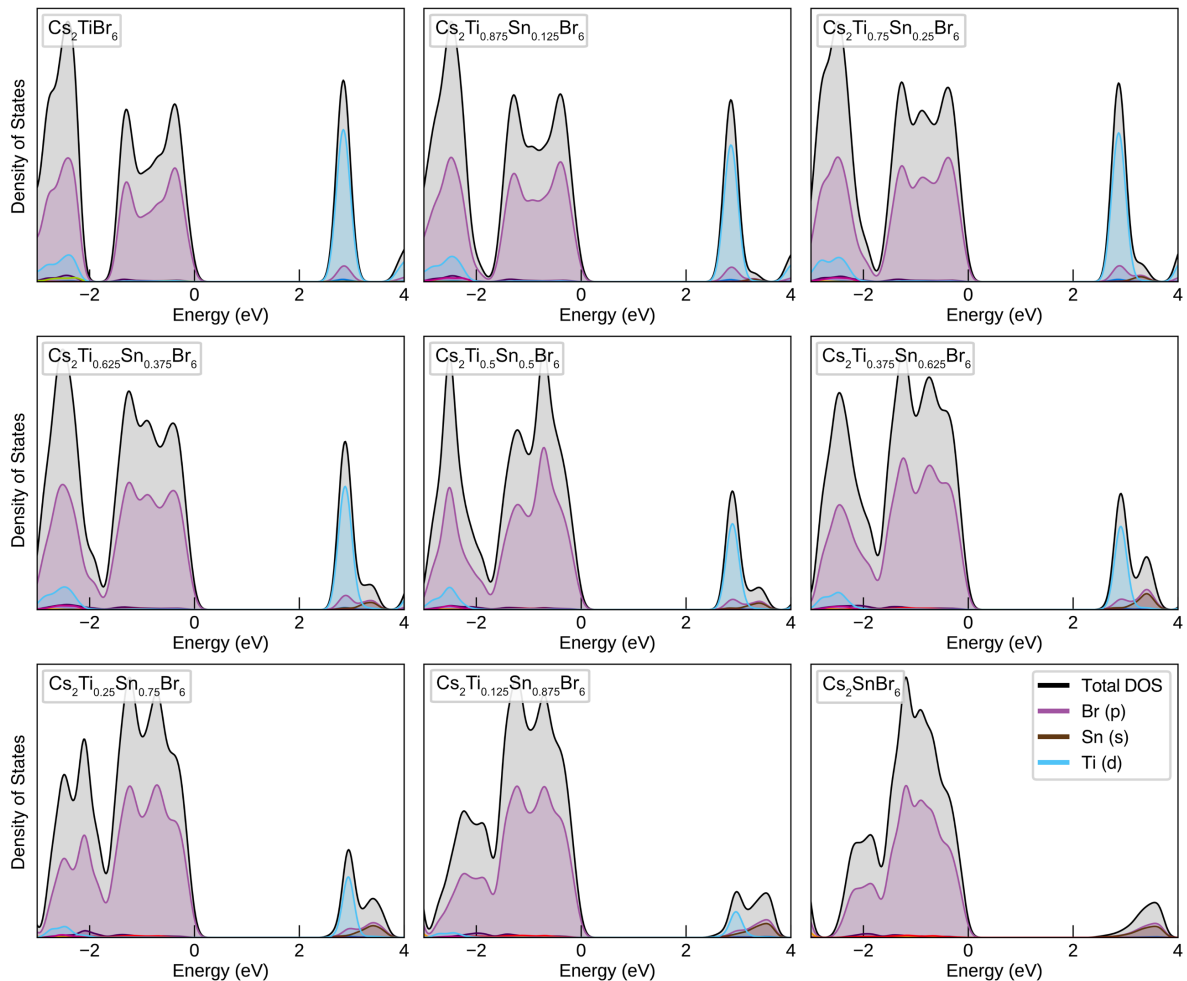


Figure S4. Calculated electronic densities of states (DOS) for $Cs_2Ti_{1-x}Sn_xBr_6$ vacancy-ordered perovskites, using hybrid DFT including spin-orbit coupling (HSE06+SOC). The valence band maximum (VBM) is set to 0 eV. DOS plots are generated using sumo,⁴ with 0.1 eV of Gaussian broadening.

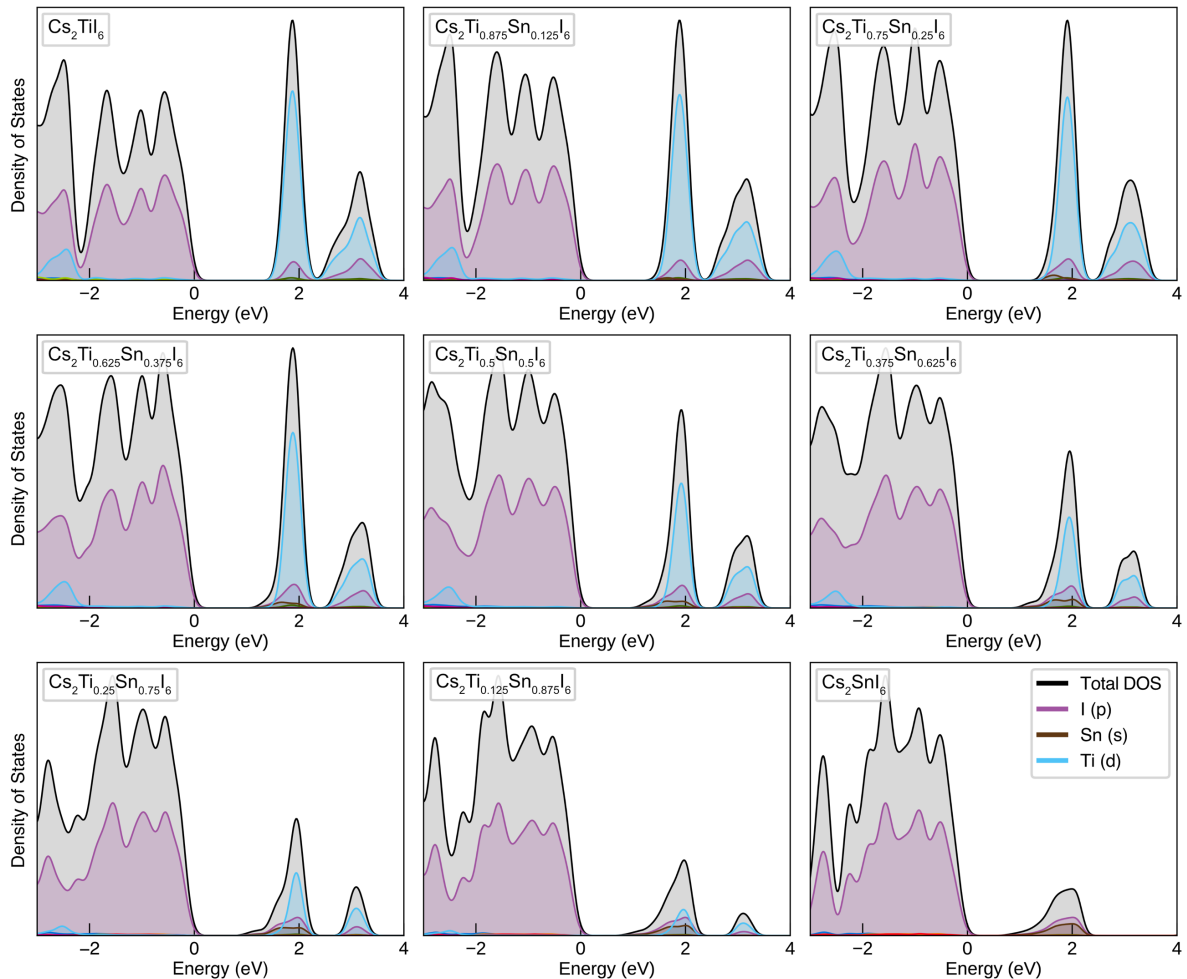


Figure S5. Calculated electronic densities of states (DOS) for $\text{Cs}_2\text{Ti}_{1-x}\text{Sn}_x\text{I}_6$ vacancy-ordered perovskites, using hybrid DFT including spin-orbit coupling (HSE06+SOC). The valence band maximum (VBM) is set to 0 eV. DOS plots are generated using sumo, with 0.1 eV of Gaussian broadening.

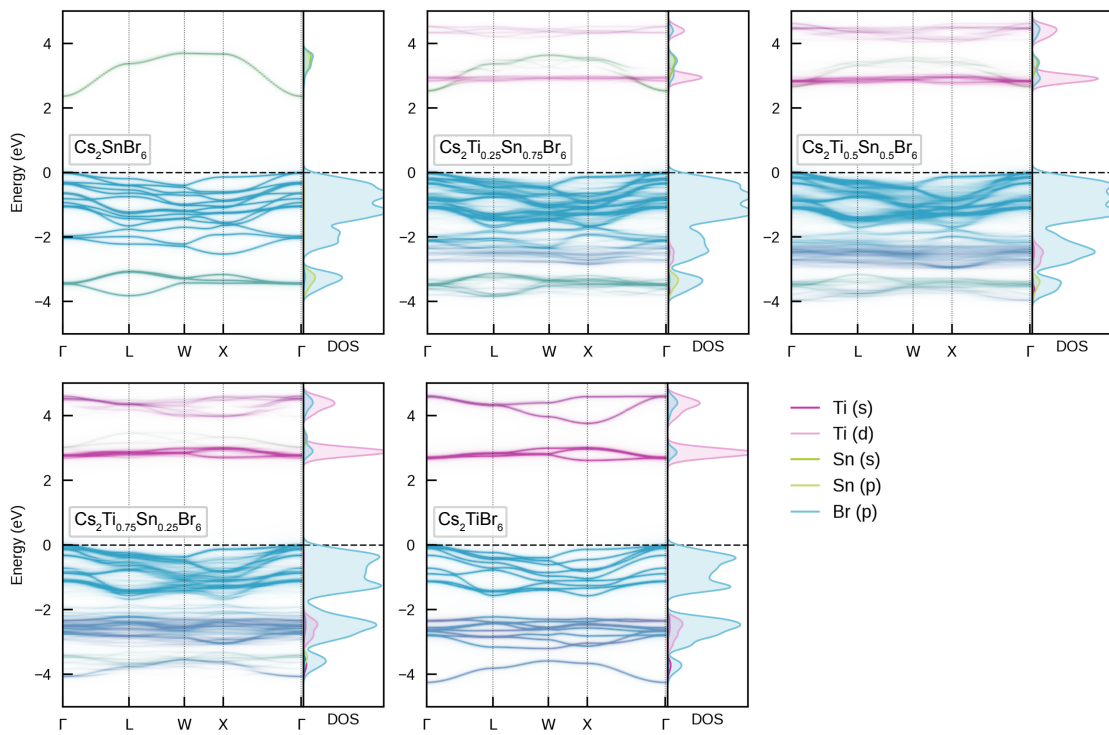


Figure S6. Unfolded electronic band structures for $\text{Cs}_2\text{Ti}_{1-x}\text{Sn}_x\text{Br}_6$ vacancy-ordered perovskites, calculated using easyunfold⁵ with hybrid DFT including spin-orbit coupling (HSE06+SOC). The valence band maximum (VBM) is set to 0 eV.

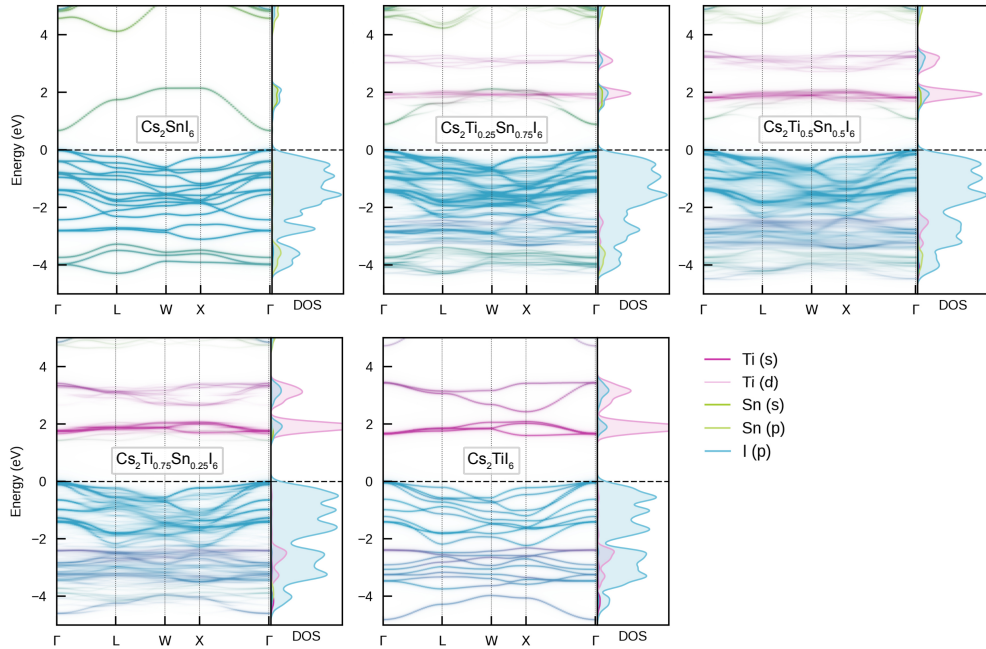
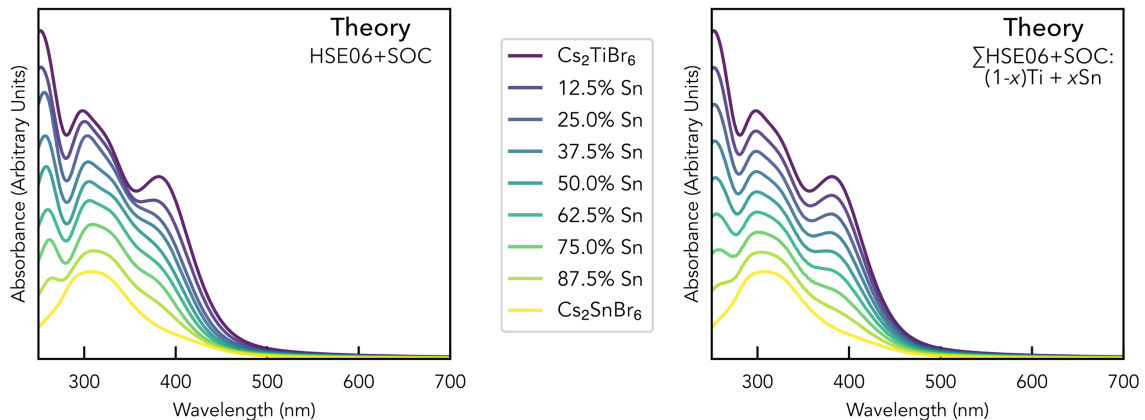


Figure S7. Unfolded electronic band structures for $\text{Cs}_2\text{Ti}_{1-x}\text{Sn}_x\text{I}_6$ vacancy-ordered perovskites, calculated using easyunfold⁵ with hybrid DFT including spin-orbit coupling (HSE06+SOC). The valence band maximum (VBM) is set to 0 eV.

$\text{Cs}_2\text{Ti}_{1-x}\text{Sn}_x\text{Br}_6$



$\text{Cs}_2\text{Ti}_{1-x}\text{Sn}_x\text{I}_6$

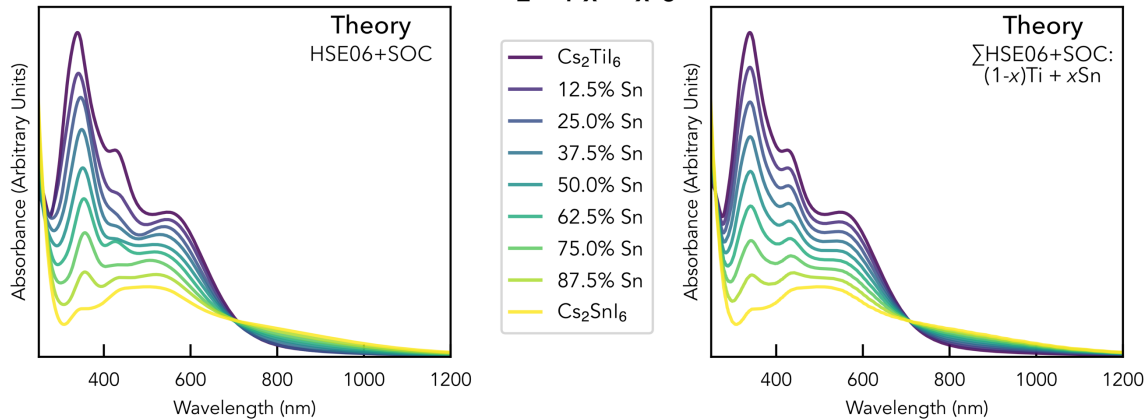


Figure S8. Computed absorption spectra of (top) $\text{Cs}_2\text{Ti}_{1-x}\text{Sn}_x\text{Br}_6$ and (bottom) $\text{Cs}_2\text{Ti}_{1-x}\text{Sn}_x\text{I}_6$ vacancy-ordered perovskites using hybrid DFT including spin-orbit coupling (HSE06+SOC). Plots on the left show the explicitly-calculated independent-particle absorption spectra of the mixed-cation supercells, while those on the right (" $\sum \text{HSE06+SOC}$ ") show the expected absorption spectra from taking a linear combination of the pure phase spectra (also computed using HSE06+SOC), reported in Kavanagh et al.² No rescaling of the spectra has been performed, and so the relative spectral intensities for different mixed compositions are physically meaningful.

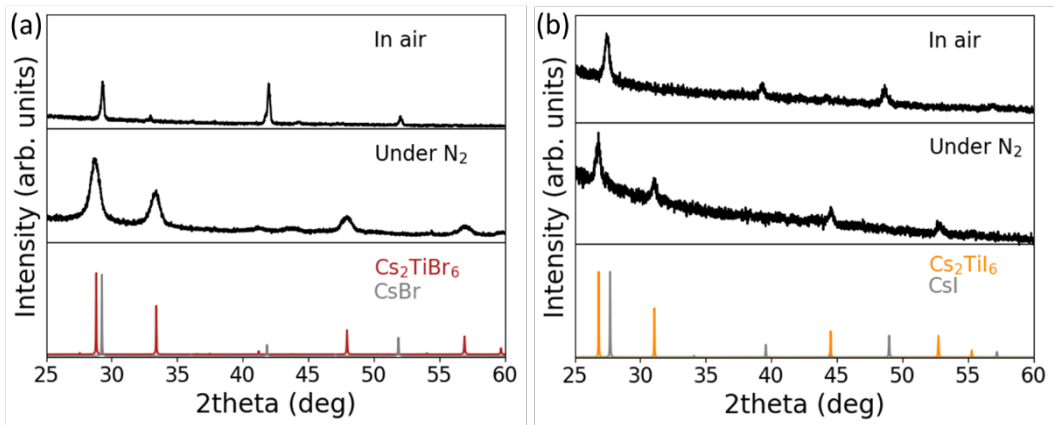


Figure S9. XRD patterns of (a) Cs_2TiBr_6 and (b) Cs_2TiI_6 under nitrogen and after air exposure.

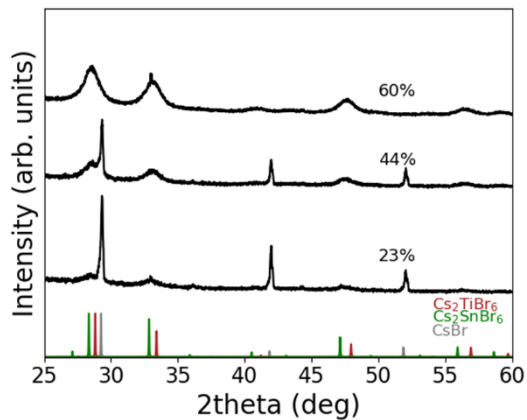


Figure S10. XRD patterns of 23%, 44% and 60% Sn alloys of $\text{Cs}_2\text{Ti}_{1-x}\text{Sn}_x\text{Br}_6$ after ~ 10 minutes in air.

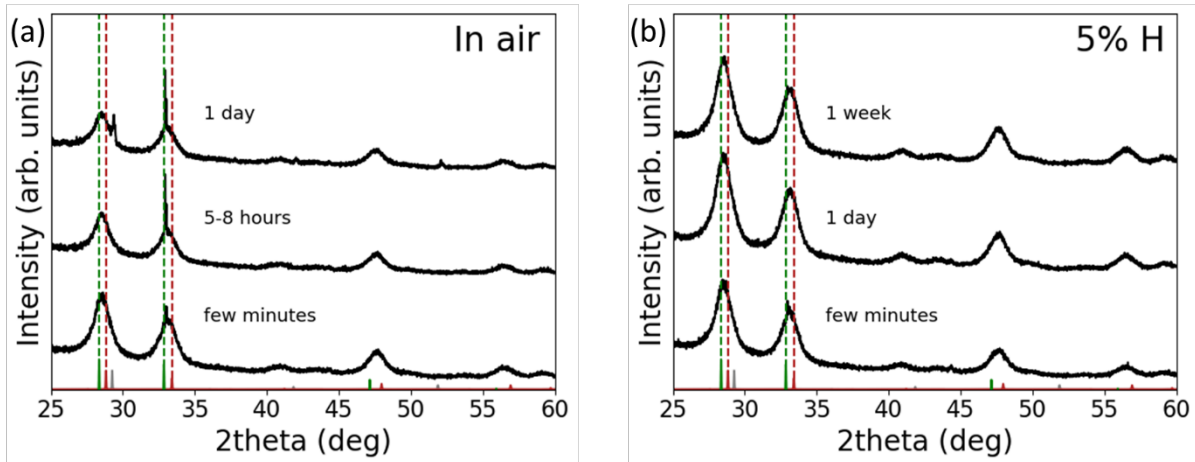


Figure S11. Evolution of measured XRD patterns for the 60% Sn alloy of $\text{Cs}_2\text{Ti}_{1-x}\text{Sn}_x\text{Br}_6$ after (a) exposure to air and (b) when stored in a desiccator with 5% humidity (H). The narrow peak at 32.97° originates from the silicon substrate.

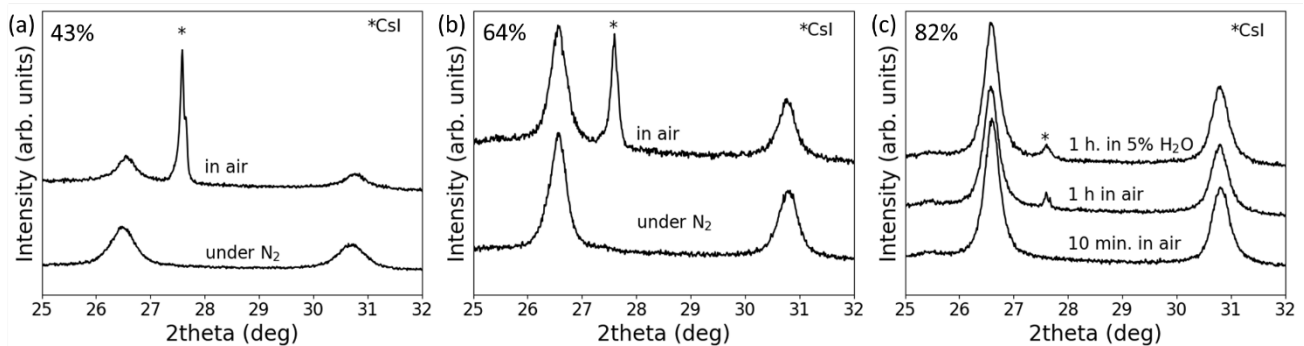


Figure S12. Stability in air of (a) 43% sample, (b) 64% sample and (c) 82% Sn alloy with chemical formula $\text{Cs}_2\text{Ti}_{1-x}\text{Sn}_x\text{I}_6\text{In}$ (c) also the stability in the 5% humidity-controlled box is shown for the 82% sample after 1 hour.

We note that with our athermal DFT model, the O_2 decomposition pathways $Cs_2MX_6 + O_2 \rightarrow MO_2 + 2CsX_3$ ($M = Ti, Sn$; $X = I, Br$) are predicted to be slightly more favourable than the $Cs_2MX_6 + O_2 \rightarrow MO_2 + 2CsX + 2X_2$ reactions shown in Table 2 (by 0.41 eV for $X = I$, and 0.57 eV for $X = Br$), in agreement with semi-local DFT calculations from the Materials Project.¹ However, both iodine and bromine are known to sublime and vaporise respectively at room temperature, which would affect the thermodynamics of these competing decomposition reactions, favouring $CsX + X_2$ over CsX_3 . CsX is the decomposition product witnessed experimentally, and we attribute this slightly lower predicted decomposition energy for CsX_3 to the neglect of finite-temperature effects and the effect of degassing iodine and bromine on the oxidation thermodynamics.

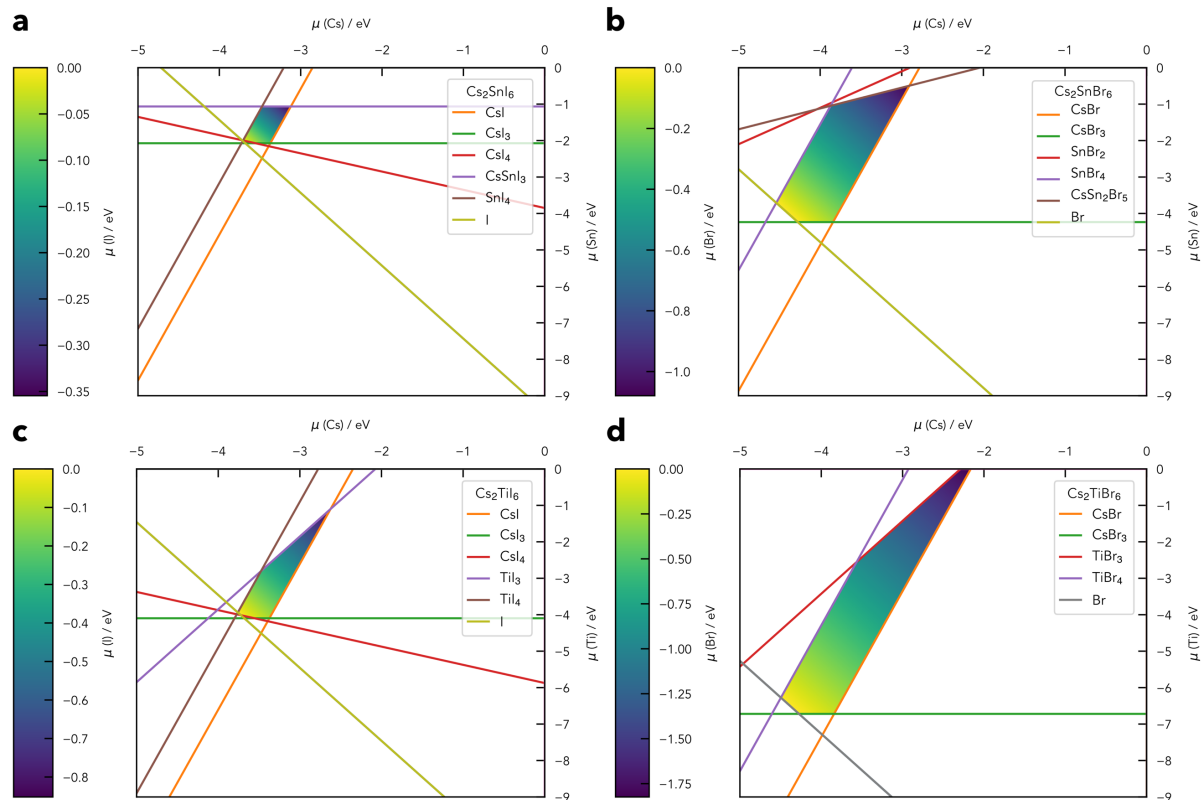


Figure S13. Calculated chemical stability regions (chemical potentials) for (a) Cs_2SnI_6 , (b) Cs_2SnBr_6 , (c) Cs_2TiI_6 and (d) Cs_2TiBr_6 vacancy-ordered perovskites, using hybrid DFT including van der Waals dispersion corrections (HSE06+D3). The halogen chemical potential is set as the dependent variable, with its chemical potential indicated by the colourmap. Bordering lines correspond to the competing phases within the $Cs-M-X$ ($M = Sn, Ti$; $X = I, Br$) chemical space.

An animation showing the changes in the electronic band structure of $Cs_2Ti_{1-x}Sn_xBr_6$ vacancy-ordered perovskites as a function of Ti fraction x is provided on the easyunfold documentation site:
<https://smtg-ucl.github.io/easyunfold>.

Mixed-cation chloride vacancy-ordered perovskites ($Cs_2Ti_{1-x}Sn_xX_6$; $X = Cl$)

In our previous work,² the pure Sn and Ti chloride vacancy-ordered perovskites were also synthesized and investigated. While these compounds were not the focus of this study, we append below the same computational analysis performed for the iodide and bromide compositions.

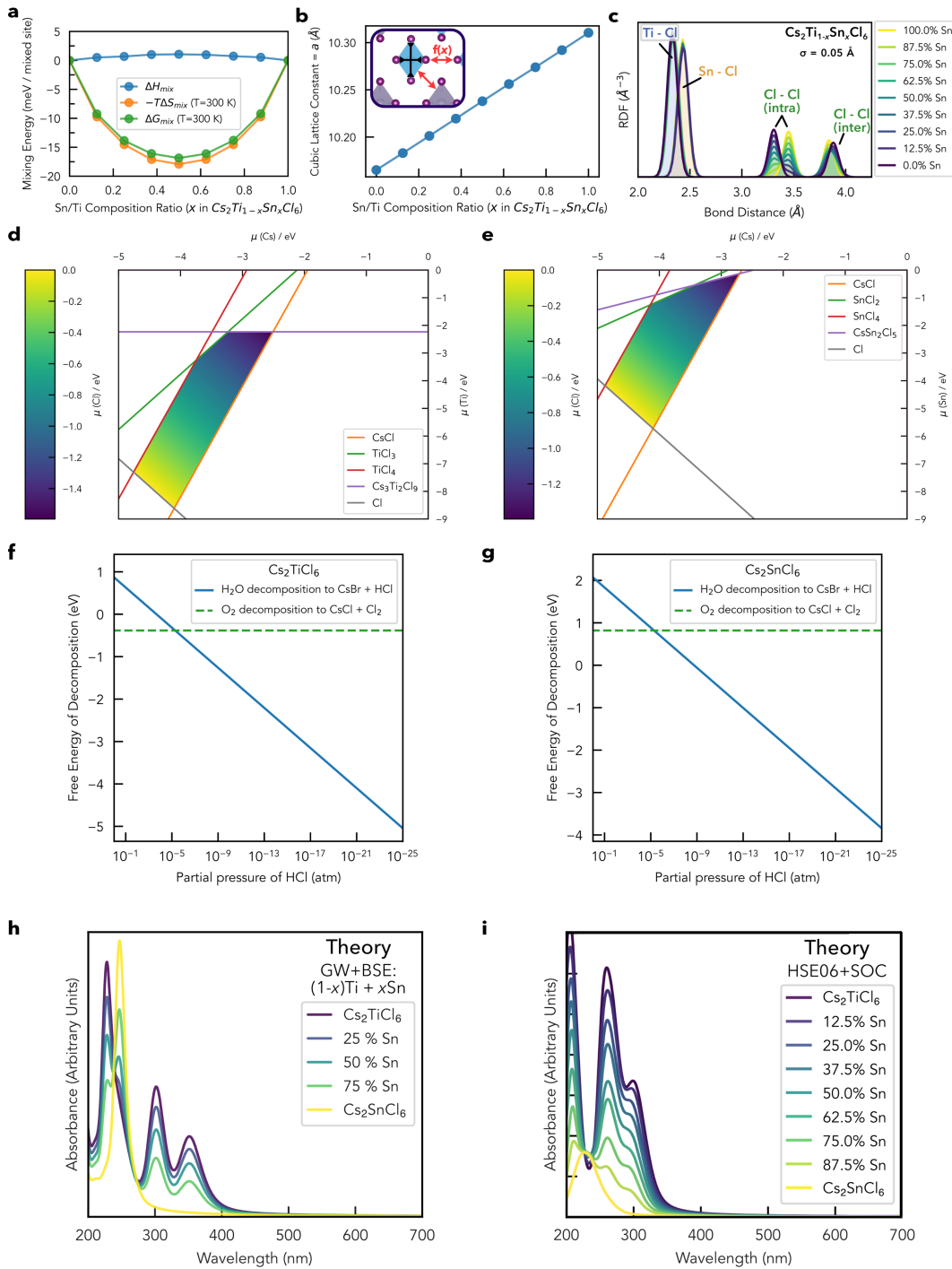


Figure S14. Computational analysis of $Cs_2Ti_{1-x}Sn_xCl_6$ vacancy-ordered perovskites. **a.** Calculated mixing enthalpies ΔH_{mix} , entropies ΔS_{mix} and free energies ΔG_{mix} as a function of the Sn/Ti composition ratio x in $Cs_2Ti_{1-x}Sn_xCl_6$ at $T = 300K$. **b.** Calculated cubic lattice constant using HSE06+D3 for $Cs_2Ti_{1-x}Sn_xCl_6$. **c.** Radial Distribution Functions (RDFs) of the Ti-X, Sn-X and Cl-Cl atomic distances in $Cs_2Ti_{1-x}Sn_xCl_6$. “intra” and “inter” refer to intra-octahedral and inter-octahedral halide-halide distances respectively. RDFs calculated using vasppy.³ **d,e.** Chemical stability regions (chemical potentials) for (d) Cs_2TiCl_6 and (e) Cs_2SnCl_6 , using hybrid DFT including van der Waals dispersion corrections (HSE06+D3). The chlorine chemical potential is set as the dependent variable, indicated by the colourmap, and bordering lines correspond to the competing phases within the $Cs-M-Cl$ ($M = Sn, Ti$) chemical space. **f,g.** Free energy of decomposition as a function of partial pressure of $HCl_{(g)}$ for (f) Cs_2TiCl_6 and (g) Cs_2SnCl_6 at $T=300K$. The partial pressure of O_2 is taken as that in air (0.2095 atm). **h, i.** Absorption spectra of $Cs_2Ti_{1-x}Sn_xCl_6$ using (h) a linear combination of the pure phase spectra computed using GW+BSE (including excitonic effects) reported in Kavanagh et al.,² and (i) explicitly-calculated independent-particle (excluding excitonic effects) absorption spectra of the mixed-cation supercells with hybrid DFT (HSE06) including spin-orbit coupling

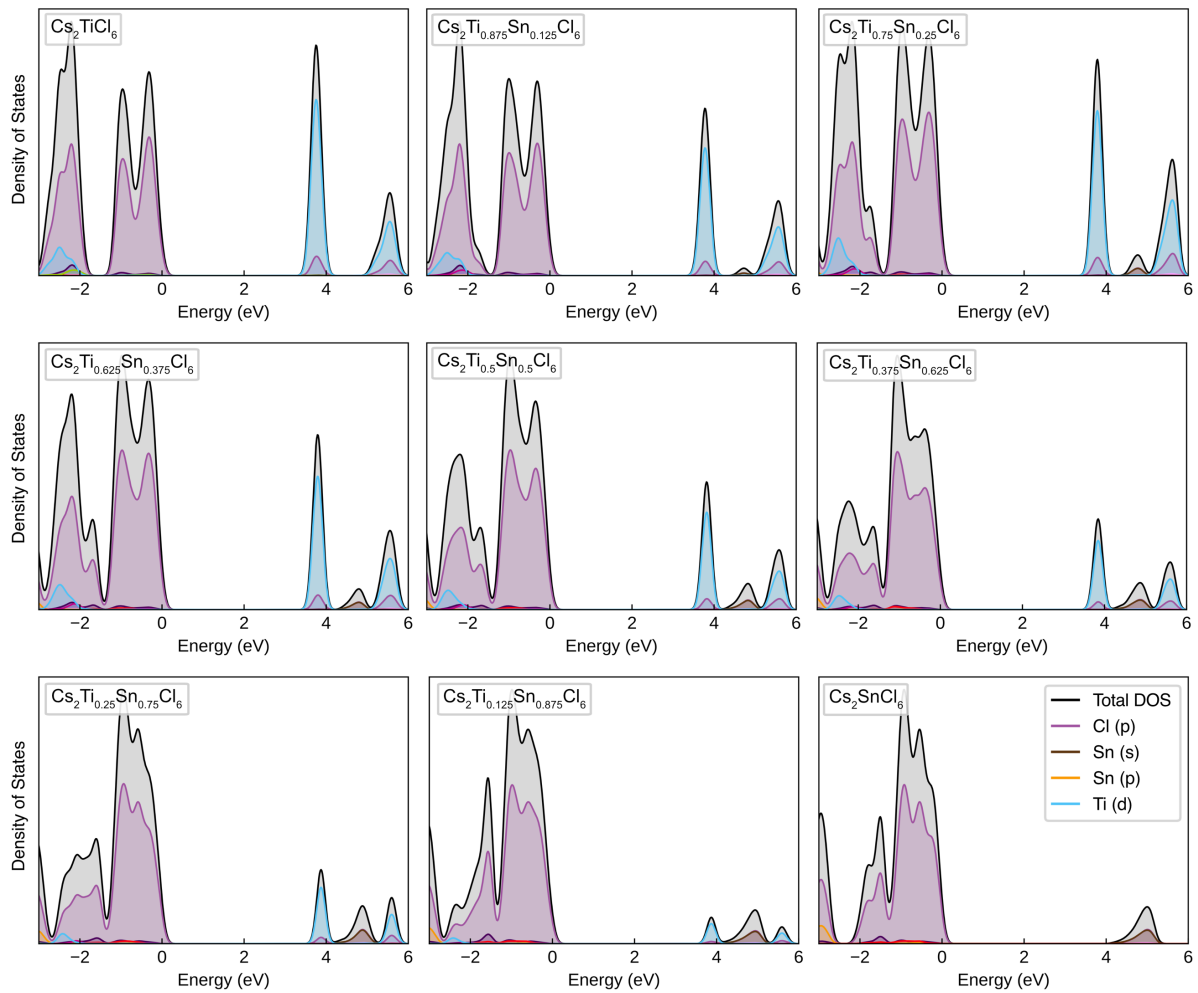


Figure S15. Calculated electronic densities of states (DOS) for $\text{Cs}_2\text{Ti}_{1-x}\text{Sn}_x\text{Cl}_6$ vacancy-ordered perovskites, using hybrid DFT including spin-orbit coupling (HSE06+SOC). The valence band maximum (VBM) is set to 0 eV. DOS plots are generated using sumo,⁴ with 0.1 eV of Gaussian broadening.

- (1) Jain, A.; Ong, S. P.; Hautier, G.; Chen, W.; Richards, W. D.; Dacek, S.; Cholia, S.; Gunter, D.; Skinner, D.; Ceder, G.; Persson, K. A. Commentary: The Materials Project: A Materials Genome Approach to Accelerating Materials Innovation. *APL Materials*. American Institute of Physics Inc. 2013. <https://doi.org/10.1063/1.4812323>.
- (2) Kavanagh, S. R.; Savory, C. N.; Liga, S. M.; Konstantatos, G.; Walsh, A.; Scanlon, D. O. Frenkel Excitons in Vacancy-Ordered Titanium Halide Perovskites (Cs_2TiX_6). *Journal of Physical Chemistry Letters* **2022**, *13* (47), 10965–10975. <https://doi.org/10.1021/acs.jpclett.2c02436>.
- (3) Morgan, B. J. Vasppy. <https://doi.org/10.5281/zenodo.8348189>
- (4) M Ganose, A.; J Jackson, A.; O Scanlon, D. Sumo: Command-Line Tools for Plotting and Analysis of Periodic Ab Initio Calculations. *Journal of Open Source Software* **2018**, *3* (28), 717. <https://doi.org/10.21105/joss.00717>.
- (5) Zhu, B.; Kavanagh, S. R. github.com/SMTG-UCL/easyunfold. github.com/SMTG-UCL/easyunfold (accessed 2023-09-14).